

Structural Dynamics by NMR in the Solid State: The Unified MOMD Perspective Applied to Organic Frameworks with Interlocked Molecules

Eva Meirovitch,* Zhichun Liang, and Jack H. Freed*

Cite This: *J. Phys. Chem. B* 2020, 124, 6225–6235

Read Online

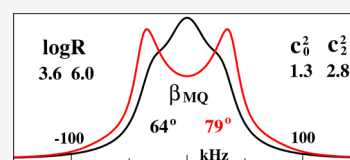
ACCESS |

Metrics & More

Article Recommendations

Supporting Information

ABSTRACT: The microscopic-order-macroscopic-disorder (MOMD) approach for NMR lineshape analysis has been applied to the University of Windsor Dynamic Materials (UWDM) of types 1, 2, α -3, β -3, and 5, which are metal–organic frameworks (MOFs) comprising mobile mechanically interlocked molecules (MIMs). The mobile MIM components are selectively deuterated crown ether macrocycles – 24C6, 22C6, and B24C6. Their motion is described in MOMD by an effective/collective dynamic mode characterized by a diffusion tensor, R , a restricting/ordering potential, u , expanded in the Wigner rotation matrix elements, $D_{0,K}^L$, and features of local geometry. Experimental ^2H lineshapes are available over 220 K (on average) and in some cases 320 K. They are reproduced with axial R , u given by the terms $D_{0,0}^2$ and $D_{0,12}^2$, and established local geometry. For UWDM of types 1, β -3, and 5, where the macrocycle resides in a relatively loose space, u is in the $1\text{--}3 kT$, R_{\parallel} in the $(1.0\text{--}2.5) \times 10^6 \text{ s}^{-1}$, and R_{\perp} in the $(0.4\text{--}2.5) \times 10^4 \text{ s}^{-1}$ range; the deuterium atom is bonded to a carbon atom with tetrahedral coordination character. For UWDM of types 2 and α -3, where the macrocycle resides in a much tighter space, a substantial change in the symmetry of u and the coordination character of the ^2H -bonded carbon are detected at higher temperatures. The activation energies for R_{\parallel} and R_{\perp} are characteristic of each system. The MOMD model is general; effective/collective dynamic modes are treated. The characteristics of motion, ordering, and geometry are physically well-defined; they differ from case to case in extent and symmetry but not in essence. Physical clarity and consistency provide new insights. A previous interpretation of the same experimental data used models consisting of collections of independent simple motions. These models are specific to each case and temperature. Within their scope, generating consistent physical pictures and comparing cases are difficult; possible collective modes are neglected.



1. INTRODUCTION

NMR lineshape analysis is a powerful method for studying structural dynamics, in particular internal molecular mobility, in the solid state.^{1–12} Internal motions are spatially restricted by the immediate molecular environment. Consequently, the NMR spectra comprise not only kinetic information associated with the motion itself but also structural information associated with the local spatial restrictions and the pertinent molecular features. In this study, we focus on rigid metal–organic frameworks (MOFs), which comprise mobile mechanically interlocked molecules (MIMs), prepared in recent years at the University of Windsor,^{13–16} hence called University of Windsor Dynamic Materials (UWDMs). The importance of gaining new insights into the dynamic structures of these materials as representatives of nanoscale MOF/MIM systems cannot be overestimated.^{17–20}

The basic UWDM design is depicted in Figure 1.¹³ The MOF is made of linking struts (green) and metal nodes (brown). The MIM comprises the axle (blue) and the wheel (red) of a [2]rotaxane linker, inserted as part of the crossbar between the struts. The wheel is a crown-ether macrocycle with thermally activated internal motion. The 24[crown]-6 ether (24C6) was used in UWDM-1,^{13,15} UWDM-2,¹⁴ α -UWDM-3,¹⁴ β -UWDM-3,¹⁴ and UWDM-5.¹⁶ The 22[crown]-6 ether (22C6) and the benzo[24]crown-6 ether (B24C6) were used in UWDM-1.¹⁵ In

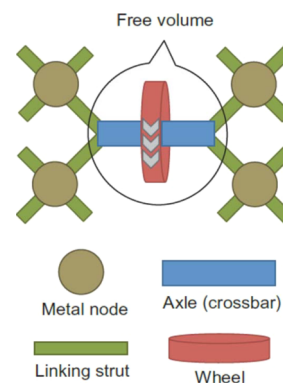


Figure 1. Basic UWDM design. The MOF is built of a combination of rigid struts (green) and metal nodes (brown). The MIM is built of the axle (blue) and the wheel (red) of a [2]rotaxane. The MIM is inserted as part of a crossbar between the struts. The axle together with the wheel is often referred to as “linker”.

Received: April 26, 2020

Revised: June 17, 2020

Published: June 25, 2020



Table 1. Compositions of the Various UWDM Systems Studied in This Work^{13–16a}

MOF	axle	macrocycle	H-bond; linker charge	strut	metal ion group ^a
UWDM-1	2[rotaxane]	[24]crown-6, B[24]crown-6, [22]crown-6	one; neutral	3,5-benzene-dicarboxylic acid groups	Cu ²⁺ , A
UWDM-2 three-fold interlocked, pillared	2[rotaxane], ADC	[24]crown-6	one; neutral	1,4-diazophenyl-dicarboxylate	Zn ²⁺ , B
α -UWDM-3 twice interlocked, pillared	2[rotaxane], BPDC, phase α	[24]crown-6	one; neutral	1,4-biphenyl-dicarboxylate	Zn ²⁺ , B
β -UWDM-3 twice interlocked, tilted pillared	2[rotaxane], BPDC, phase β	[24]crown-6	one; neutral	1,4-biphenyl-dicarboxylate	Zn ²⁺ , A
UWDM-5 asymmetric paddle-wheels	Y-shaped with 2,4,5-triphenylimidazolium end-groups	[24]crown-6	two; cationic (balanced by the nitrate)	[Zn(NO ₃)(DEF)] secondary building units ¹⁶	Zn ²⁺ , A

^aGroup A (B): The macrocycle resides in relatively loose (tight) spaces. ADC: 4,4'-azodiphenyldicarboxylic acid;¹⁴ BPDC: 4,4'-biphenyldicarboxylic acid;¹⁴ DEF: diethylformamide.¹⁶

addition to the identity of the macrocycle, these materials differ in the chemical composition of the axle and paddle-wheels; this information appears in Table 1. Isotope labeling of the macrocycles was carried out using deuterium gas for hydrogenation of the crown-ether double bond (*E* and *Z* isomers).¹³ Deuterium lineshapes were acquired in previous work over temperature ranges of 220 K (on average) and in some cases as extended as 320 K.^{13–16}

The authors of refs 13–16 studied macrocycle mobility in these materials with ²H lineshape analysis. They used the multi-simple-mode (MSM) method, which combines several independent simple local motional modes and neglects possible collective modes. However, it was shown that while each simple mode can well be fast in the Redfield sense, collective modes being necessarily slower can dominate the NMR lineshapes.^{21,22}

Two-site jumps of the C–D bonds around axes allowed to vary as a function of system and temperature and quite unique macrocycle motions involving subsets of the crown-ether atoms were considered. To reconcile the fact that the four double-bond *E* and *Z* isomers yield the same experimental spectra, quite specific local geometry had to be postulated to render the overall model plausible. In MSM, the spatial restrictions are implicit in the geometric features; ordering potentials, necessarily exerted by the solid matrix, are not included in the formalism. With enough independent modes included, MSM yielded good agreement between calculated and experimental ²H lineshapes.^{13–16}

In themselves, the MOF/MIM systems described above are not “molecular machines” or “molecular switches”; these functions require a reversible change in structure and/or dynamics. However, the results of consistent analyses of structural dynamics could serve as reference for devising nanodevices. For this, one has to be able to compare the relevant physical parameters among systems. This is difficult to achieve with collections of simple geometrically unrelated dynamic modes, where model improvement means adding degrees of freedom by including additional simple motional modes; this changes the overall model, further limiting comparison. Finally, often, MSM models present more details than can unambiguously be discerned from just the NMR lineshapes.

We have developed the microscopic-order-macroscopic-disorder (MOMD) approach²³ for the analysis of ²H lineshapes from polycrystalline samples.^{8,24–27} MOMD is a mesoscopic model, largely free of the above-noted limitations. It is based on the stochastic Liouville equation (SLE) developed by Freed and

co-workers for generally treating restricted motions.^{28–30} All of the major features – type of motion, spatial restrictions, and local geometry – are treated for the entire motional range with due consideration to their three-dimensional tensorial requirements. The motion is expressed by a diffusion tensor, *R*, the spatial restrictions by a potential, *u*, expanded in the basis set of the real combinations of the Wigner rotation matrix elements (which are in direct proportion to the spherical harmonics), and the local geometry by the relative orientation of the model and the NMR tensors. These elements describe an effective/collective restricted local-motional mode. Model improvement is accomplished in a straightforward manner by enhancing the local potential and/or lowering the symmetry of the diffusion, ordering, and/or magnetic tensors.

Previously, we applied MOMD to the analysis of ²H lineshapes with the C–D bond serving as probe; the systems studied include medium-sized molecules,^{24,27} globular proteins,⁸ and the core region of several dry and hydrated β ₄₀-amyloid-fibrils.^{25,26} In all of these cases, an axial *R*, *u* given by the terms *D*_{0,0}² and *D*_{0,2|2}², and simple descriptions of the local geometry proved to be an appropriate parameter combination.

It is important to appreciate the useful “information content” of the MOMD lineshapes. There are undoubtedly many atomistic details as well as orienting or “cage” effects that can lead to a particular MOMD lineshape. Our previous and present successful use of the MOMD model shows that it contains enough relevant features that represent in a collective sense the dominant slower structural dynamics that remains after faster local “atomistic” modes average out in the NMR timescale. MOMD is no substitute for detailed theoretical analyses from first principles of NMR relaxation that are emerging.^{31,32} However, MOMD is a good mesoscopic approach with a clear physical interpretation that realistically represents the inherently limited (partly in view of the polycrystalline morphology) information content of solid-state NMR lineshapes.

Here, we apply MOMD to the intricate MOF/MIM systems described above, for which experimental ²H spectra^{13–16} are available over extensive temperature ranges. In general, the parameter combination found to be appropriate in previous cases reproduces the main features of the experimental ²H NMR spectra. Our analysis is aimed at capturing the common physical characteristics and pinpointing the distinctive ones; this approach serves well the long-term goal of this study – to help design nanodevices.

On the basis of this rationale, two groups are distinguished. UWDM-1, β -UWDM-3, and UWDM-5 with 24C6, as well as

UWDM-1 with 22C6 and B24C5, form group A,^{13–16} where the macrocycle resides in a relatively loose space. The ²H spectra of the constituents of group A evolve with increasing temperature similarly, however, at a different pace. This evolution is characterized in the upcoming sections in terms of MOMD parameters; the different pace is ascribed to different activation energies for local motion. UWDM-2 and α -UWDM-3 with 24C6 form group B, where the macrocycle resides in a tight space.¹⁴ Below 276 K, the group B spectra evolve similar to the group A spectra. Above 276 K, they evolve in a qualitatively different manner, ascribed to a change in the form/symmetry of the local potential and the coordination character of the deuterium-bonded carbon atom.

In Section 2, we briefly summarize the MOMD theory. In Section 3, we illustrate the sensitivity of MOMD in the relevant parameter ranges and carry out MOMD analysis of representative experimental ²H spectra from groups A and B. Our conclusions appear in Section 4.

2. THEORETICAL BACKGROUND

The MOMD theory as applied to NMR was described previously.^{8,24–27} For convenience, its basics are outlined below. Figure 2 shows the MOMD frame structure for the

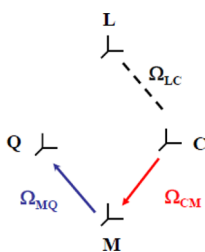


Figure 2. MOMD frame structure. L – space-fixed laboratory frame; C – molecule-fixed local director; M – probe-fixed ordering/diffusion frame; Q – probe-fixed magnetic frame. The Euler angles Ω_{CM} are time-dependent due to molecular motion, the Euler angles Ω_{MQ} are time-independent, and the Euler angles Ω_{LC} are distributed in space at random.

deuterium nucleus. L is the space-fixed laboratory frame, and C is the local director frame fixed in the molecule. M denotes the principal axis system (PAS) of the local ordering tensor, S , taken the same (for simplicity) as the PAS of the local diffusion tensor, R . Q denotes the PAS of the quadrupolar tensor. The M and Q frames are fixed in the probe (in this case, the C–D bond).

The Euler angles Ω_{CM} are time-dependent due to the local motion of the probe. The Euler angles $\Omega_{MQ} = (\alpha_{MQ}, \beta_{MQ}, \gamma_{MQ})$ are time-independent. Given that the Q frame is axially symmetric, one has $\gamma_{MQ} = 0$. For convenience, the angle α_{MQ} is set equal to zero. Thus, the orientation of Z_M (main ordering/diffusion axis) relative to Z_Q (the principal axis of the quadrupolar tensor pointing along the C–D bond) is given by the polar angle, β_{MQ} , often called “diffusion tilt”.

The stochastic Liouville equation (SLE) for a particle diffusing in an anisotropic medium, for the special case where the director is parallel to the applied magnetic field ($\Omega_{LC} = 0$), is given by²⁸

$$\left(\frac{\partial}{\partial t}\right)\rho(\Omega, t) = [-i\mathcal{H}(\Omega)^X - \Gamma_\Omega]\rho(\Omega, t),$$

$$\text{with } \Gamma_\Omega P_0(\Omega) = 0 \quad (1)$$

The Euler angles $\Omega \rightarrow (\alpha, \beta, \gamma)$ are the same as Ω_{CM} in the notation above. Γ_Ω is a Markovian operator for the rotational reorientation of the spin-bearing moiety (probe). $\mathcal{H}(\Omega)^X$ is the quantum Liouville operator, i.e., the commutator superoperator defined in terms of $\mathcal{H}(\Omega)$, the probe spin Hamiltonian describing the magnetic interactions. $P(\Omega, t)$ is the probability of finding Ω in the particular state at time, t , and $P_0(\Omega)$ is the unique equilibrium probability distribution of $P(\Omega, t)$ defined by $\Gamma_\Omega P(\Omega, t) = 0$. $\rho(\Omega, t)$ is the density matrix operator describing the joint evolution of the quantum spin degrees of freedom and the classical motion coordinates, Ω .

A simple form of the diffusion operator, Γ_Ω , is²⁸

$$-\Gamma_\Omega = R\Delta_\Omega^2 P(\Omega, t) - (R/kT)(\sin\beta)^{-1}\partial/\partial\beta[\sin\beta \mathbf{T}P(\Omega, t)] \quad (2)$$

where R is the isotropic rotational diffusion rate, ∇_Ω^2 is the rotational diffusion operator in the Euler angles, Ω , and \mathbf{T} is the restoring torque. The latter is equal to $\partial u/\partial\beta$ for an axial restoring potential, e.g., $u \cong (-3/2)c_0^2(\cos\beta)^2$ (u is given in units of kT ; i.e., it is dimensionless). The expression of Γ_Ω for rhombic diffusion tensors and rhombic potentials is given in ref 29. Reference 30 comprises the extension of the theory to arbitrary Ω_{LC} .

In polycrystalline morphologies to which we refer here, there is no “macroscopic order” aligning the molecules. Therefore, one has to calculate ²H NMR spectra for a large enough number of director orientations (i.e., Ω_{LC} values) and sum the individual lineshapes according to random distribution; this completes the MOMD model.^{8,23}

In this study, we are using an axial diffusion tensor, R , associated in the absence of a restricting potential with three decay rates, $\tau_K^{-1} = 6R_\perp + K^2(R_\parallel - R_\perp)$, where $K = 0, 1, 2$ (K is the order of the rank 2 diffusion tensor). R_\parallel and R_\perp are the principal values of R ; one may also choose to define $\tau_\parallel = 1/(6R_\parallel)$ and $\tau_\perp = 1/(6R_\perp)$.²⁹

For a uniaxial local director, one may expand the potential in the complete basis set of the Wigner rotation matrix elements with $M = 0, D_{0,K}^L(\Omega_{CM})$. One has^{28–30}

$$u(\Omega_{CM}) = \frac{U(\Omega_{CM})}{kT} = - \sum_{L=1}^{\infty} \sum_{K=-L}^{+L} c_K^L D_{0,K}^L(\Omega_{CM}) \quad (3)$$

with c_K^L being dimensionless. If only the lowest, $L = 2$, terms are kept, one obtains the real potential^{29,30}

$$u(\Omega_{CM}) = -c_0^2 D_{0,0}^2(\Omega_{CM}) - c_2^2 [D_{0,2}^2(\Omega_{CM}) + D_{0,-2}^2(\Omega_{CM})] \quad (4)$$

This form of $u(\Omega_{CM})$ is used below. Note that we did not consider the lowest $L = 1$ terms. They could be considered³³ but are typically omitted in view of the second-rank ($L = 2$) nature of the quadrupolar tensor.³⁴

The order parameters for $L = 2$ are defined as²⁹

$$\langle D_{0,K}^2(\Omega_{CM}) \rangle = \int d\Omega_{CM} D_{0,K}^2(\Omega_{CM}) \exp[-u(\Omega_{CM})] / \int d\Omega_{CM} \exp[-u(\Omega_{CM})],$$

$$K = 0, 2 \quad (5)$$

For at least three-fold symmetry around the local director, C, and at least two-fold symmetry around the principal axis of the

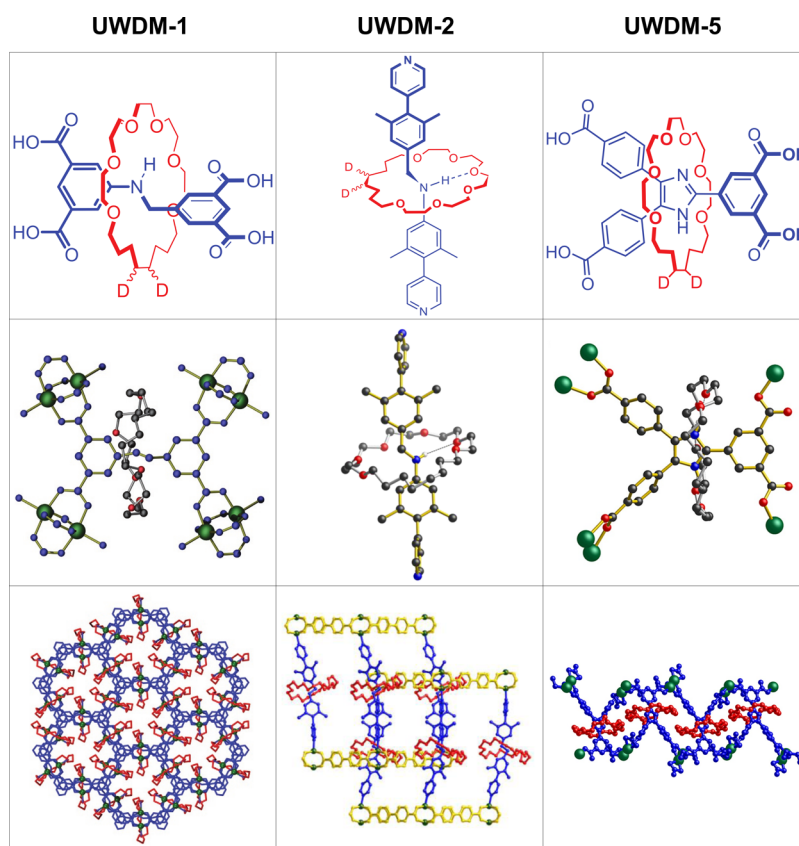


Figure 3. Neutral linkers UWDM-1/24C6, UWDM-2/24C6, and UWDM-5/24C6. Upper part: schematic molecular drawing. Middle part: ball-and-stick representations of a single unit of the respective MIM coordinated to the metal-ion-containing paddle-wheels or in the pillaring framework of UWDM-5 to the zinc dicarboxylate layers. Lower part: location of the macrocycle in the respective 3D metal–organic framework. Reproduced with permission from refs 13, 14, and 16. Copyrights 2012, 2014, and 2016 of the American Chemical Society.

local ordering tensor, Z_M , only the irreducible tensor components $S_0^2 \equiv \langle D_{0,0}^2(\Omega_{CM}) \rangle$ and $S_2^2 \equiv \langle D_{0,2}^2(\Omega_{CM}) + D_{0,-2}^2(\Omega_{CM}) \rangle$ survive.²⁹ The Saupe order parameters relate to S_0^2 and S_2^2 as $S_{xx} = (\sqrt{3/2}S_2^2 - S_0^2)/2$, $S_{yy} = -(\sqrt{3/2}S_2^2 + S_0^2)/2$, and $S_{zz} = S_0^2$.

The implementation of the MOMD approach in terms of an effective computer program is described in refs 23 and 35. Reference 35 is a User's Guide for the calculation of slow-motional magnetic resonance spectra (in this case, ^2H spectra) for given values of Ω_{LC} . Reference 23 is the article where MOMD was originally developed; the superposition of individual slow-motional lineshapes according to random distribution of Ω_{LC} is discussed in some detail in that article.

To carry out a MOMD calculation, one has to specify the external magnetic field, the quadrupole constant, Q , the intrinsic linewidth, $(1/T_2)^*$, the number of Ω_{LC} values for which slow-motional lineshapes are to be calculated, and the technical parameters associated with the calculation of slow-motional (NMR or ESR) spectra.³⁵ The physical parameters to be specified and varied in data analysis include the coefficients c_0^2 and c_2^2 of the potential of eq 4 and the diffusion rate constants R_{\parallel} and R_{\perp} . The diffusion tilt, β_{MQ} , is typically fixed at a preset value.

3. RESULTS AND DISCUSSION

3.1. Systems Studied. Figure 1 shows the basic UWDM design. UWDM-1 comprises linkers with symmetrical paddle-wheels and the crown ethers 24C6, 22C6A, and B24C6 (Figure S1a,c of the Supporting Information) as wheels. UWDM-5 with

24C6 acting as a wheel comprises nonsymmetrical paddle-wheels. The UWDM-2 and UWDM-3 frameworks are interpenetrated (UWDM-2, three-fold and UWDM-3, two-fold), with the 24C6 rings of the MIM positioned inside the tight (square) openings of neighboring zinc dicarboxylate layers (Figure S1d of the Supporting Information).¹⁴ Upon activation (i.e., initiation of wheel dynamics) of UWDM-3 by removing solvent, a reversible phase transformation occurs: α -UWDM-3 denotes the system before and β -UWDM-3 after the phase transition. In β -UWDM-3, a tilted pillared structure, where the macrocycle resides no longer in a tight space, is established. Table 1 summarizes the structures of the UWDMs studied. Group A (B) comprises MOF/MIM systems where the macrocycle resides in relatively loose (tight) spaces.

Figure 3 illustrates the information given in Table 1. The upper part shows the neutral linkers of UWDM-1/24C6 (refs 13 and 15, UWDM-2/24C6 (ref 14, and UWDM-5/24C6 (ref 16). The middle part shows ball-and-stick representations of single units of these MIMs coordinated to the metal ions in the paddle-wheels or, in the case of the pillaring framework of UWDM-5, to the zinc dicarboxylate layers. The lower part shows the location of the macrocycle in the respective 3D metal–organic frameworks. Figure S1 of the Supporting Information provides additional illustration.

The design criteria for the UWDM systems are specified in ref 13, where the synthesis of UWDM-1 and the X-ray structural characterization of the MOF linker comprising the 24C6 wheel are delineated. The experimental observation by solid-state NMR of the motion of 24C6 inside UWDM-1 is also described

in that article; similar descriptions appear in refs 14–16 for the other MOF/MIM systems. Among others, it is indicated that the temperature was calibrated using ^{207}Pb NMR spectra of PbNO_3 acquired under the same conditions, following literature methods. The preparation of UWDM-2 and UWDM-3 and the conditions under which one obtains α -UWDM-3 or β -UWDM-3 are described in ref 14. The synthesis of the linkers that contain the macrocycles 22C6 and B24C6 is described in ref 15. The preparation of UWDM-6 is described in ref 16.

3.2. General Assessments.

- (a) Low-temperature ^2H NMR spectra with a Pake-doublet appearance, which are unchanged upon increasing the temperature over a sizable range, are considered to be rigid-limit (RL) spectra. They are characterized by an axial ^2H quadrupole tensor with a principal value of $Q \cong 160$ kHz. In all of our calculations, we used $Q = 160$ kHz and an intrinsic linewidth, $(1/T_2)^*$, of 1 kHz.
- (b) The strength of the local potential is estimated semi-quantitatively as follows. Let us assume exchange between equally populated sites ($p_1 = p_2$). In the extreme motional narrowing limit, one has $1/T_2 = \delta^2 \times (p_1 \times p_2)/k_{\text{ex}} (1/T_2)$, linewidth; δ , chemical-shift site-separation; k_{ex} , jump/exchange rate). Very fast diffusive motion yields $1/T_2 = \Delta^2 \times (S_0^2)^2 \times \tau$ for the simple potential $u = -c_0^2 D_{00}^2$ (Δ , axial magnetic tensor anisotropy; $S_0^2 = \langle D_{00}^2 \rangle$; $\tau = 1/(6R)$, correlation time for local motion). Thus, in the limit of very fast local motion, $(S_0^2)^2$ in MOMD is formally analogous to $p_1 \times p_2$ in the exchange process. For $p_1 = p_2$, one has $p_1 \times p_2 = (S_0^2)^2 = 0.25$, which corresponds to $c_0^2 = 2.3$; 29 for $p_1 \neq p_2$, one has $(S_0^2)^2 < 0.25$, which corresponds to $c_0^2 < 2.3$. It is reasonable to assume that c_2^2 is comparable to c_0^2 ; thus, both coefficients are expected to represent potentials on the order of 2–3 kT .
- (c) The [2]rotaxane wheel was labeled with deuterium at the double bond of the crown ether (*E* and *Z* isomers). Let us consider several cases of C–D diffusion about axes of stereochemical relevance. For deuterium bonded to a carbon atom with double-bond character (ideally, D=C=C), the C–H and C–D bonds of a given methylene group (only one H-atom is isotope-labeled) lie in the same plane. Two-site exchange would occur about a jump axis tilted at 60° (or 120°) from the C–D bond; this corresponds to a diffusion axis tilted at 64° (or 133°) from the C–D bond. 37 For deuterium bonded to tetrahedral carbon, diffusion occurs around the symmetry axis of the tetrahedron; in this case, the diffusion axis is tilted at 70.5° (or 109.5°) from the C–D bond. For the 12[crown]-4 ether in its LiNCS complex, the tilt angle between the C–D bond and the axis for internal motion was determined to be equal to 79° (or 101°). 36 We consider β_{MQ} equal to 64, 70, or 79° to be possible values for the diffusion tilt.
- (d) R_{\parallel} represents motion around the main ordering/diffusion axis, z , and R_{\perp} represents motion around the (equal) x and y axes, which are perpendicular to z . We show below that R_{\parallel} may be associated with C–D motion and R_{\perp} with macrocycle motion.

3.3. MOMD Simulations. As indicated, the potential coefficients c_0^2 and c_2^2 are expected to be on the order of 1–3 (in the unit of kT). For a quadrupole constant of 160 kHz, the analysis is sensitive to $\tau_{\perp} = 1/(6R_{\perp})$ and $\tau_{\parallel} = 1/(6R_{\parallel})$ in the millisecond-to-microsecond range, i.e., to $\log R_{\parallel}$ and $\log R_{\perp}$

(which are the parameters we report) in the 2–7 range. As indicated, the angle β_{MQ} is taken to be equal to 64, 70, or 79° .

Figure 4 shows MOMD spectra of the kind that is expected at lower temperatures, obtained with $Q = 160$ kHz, $\beta_{\text{MQ}} = 70.5^\circ$,

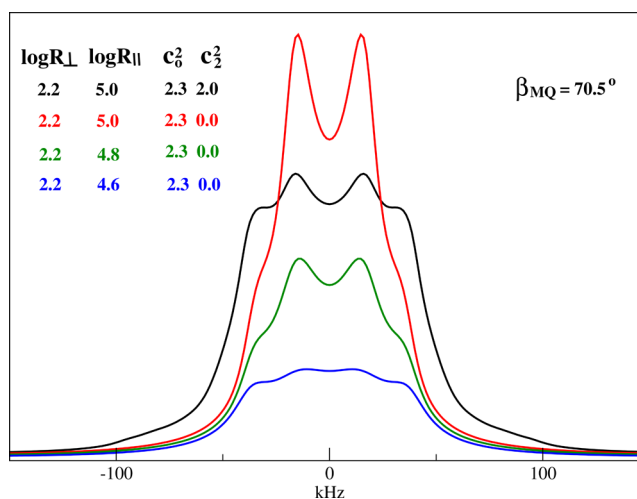


Figure 4. Calculated MOMD spectra for local diffusion rate constants, R_{\perp} and R_{\parallel} , given in logarithmic form; coefficients, c_0^2 and c_2^2 , of the local potential of eq 4; and diffusion tilt angle, β_{MQ} , with values as depicted in the figure. Additional parameters include a quadrupole constant of 160 kHz and an intrinsic linewidth, $(1/T_2)^*$, of 1 kHz.

$\log R_{\perp} = 2.2$, and $\log R_{\parallel}$ in the 4.6–5.0 range. As the symmetry of the local potential is not known, we consider both the axial case, represented by $c_0^2 = 2.3$ and $c_2^2 = 0$, and rhombic case, represented by $c_0^2 = 2.3$ and $c_2^2 = 2$. The red, green, and blue traces correspond to the axial potentials. They are quite sensitive to R_{\parallel} ; all of them exhibit an overall spectral width on the order of 80 kHz. However, the lower-temperature experimental spectra have overall widths close to 240 kHz ($3/2Q$), which corresponds to the RL spectrum (see below). Thus, axial local potentials are inappropriate. On the other hand, the black spectrum in Figure 4, which corresponds to a rhombic potential, has an overall width on the order of 180 kHz, which could well be an incipient slow-motional lineshape. In our subsequent simulations, we allow for rhombic potentials.

Figure 5 shows series of ^2H lineshapes obtained with β_{MQ} equal to 64 (black) and 79° (red), which we take as lower and upper bounds for β_{MQ} . Increasing R_{\parallel} and R_{\perp} and decreasing c_0^2 and c_2^2 in the series a–i simulate a typical scenario of increasing temperature. Clearly, the local geometry represented by the angle β_{MQ} has a substantial effect on the analysis. The $\beta_{\text{MQ}} = 64^\circ$ spectra (black) appear to “lag behind” the $\beta_{\text{MQ}} = 79^\circ$ spectra (red). This is consistent with the activation barrier being higher when the deuterium-bonded carbon has double-bond character ($\beta_{\text{MQ}} = 64^\circ$). Figures S2, S3, and S5–S7 of the Supporting Information show the full spectrum evolution with temperature for the various MOF/MIM systems. In general, the lineshapes change slowly with temperature (for example, see Figure S7 of the Supporting Information).

Figure 6 features intermediate diffusion rate constants, R_{\parallel} and R_{\perp} , and u in the 1–3 range. It illustrates the emergence of a “shoulder” as a consequence of just a small variation in R_{\parallel} and R_{\perp} ; the relevance of this feature will become clear shortly.

3.4. MOMD Analysis. **3.4.1. Qualitative Analysis.** Figure 7a–c shows selected ^2H NMR spectra from UWDM-1, UWDM-5, and β -UWDM-3 with 24C6 (group A) obtained at

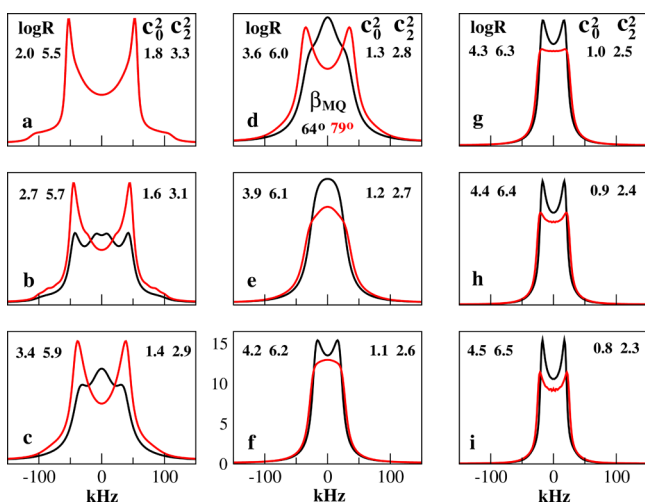


Figure 5. Illustration of the evolution of ^2H MOMD spectra in the parameter range of interest for a scenario that simulates an increase in temperature from a to i. The black lineshapes are for $\beta_{\text{MQ}} = 64^\circ$ and the red lineshapes for $\beta_{\text{MQ}} = 79^\circ$. $\log R_\perp$, $\log R_\parallel$, c_0^2 , and c_2^2 as depicted in the figure. The definition of the various parameters and additional information used in these calculations are the same as in the caption of Figure 4.

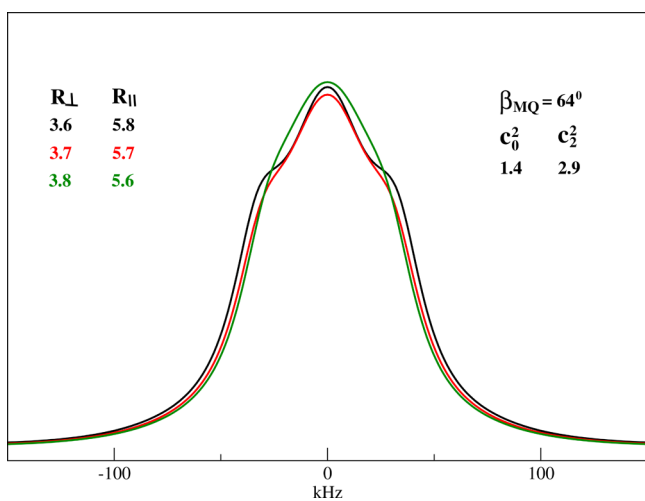


Figure 6. Calculated MOMD spectra for $\log R_\perp$, $\log R_\parallel$, c_0^2 , c_2^2 , and β_{MQ} as depicted in the figure. The definition of the various parameters and additional information used in these calculations are the same as in the caption of Figure 4.

the same or nearly the same temperatures. In some cases, such lineshapes closely resemble one another. Occasionally, pairs of such spectra have a similar appearance, with one of the constituents exhibiting narrower overall width; this is ascribed to fast local fluctuations that reduce the rigid-limit ^2H quadrupole constant to a somewhat smaller effective value.^{13–16} In other cases, similar lineshapes of different systems appear at different temperatures; this is ascribed to different activation energies for local motion. A broad pattern appears at lower temperatures in some of the overall-similar lineshapes – cf. the 255 K spectrum in row b as compared to the 251 K spectrum in row a of Figure 7. Its edges, occurring at $\pm 3/8Q$, correspond to the perpendicular component of the static quadrupole tensor; often, they are dubbed shoulders. As shown in Figure 6, the shoulder-pattern may be ascribed to a relatively small change in R_\perp or R_\parallel . It will not be seen in given systems if experimental spectra are not

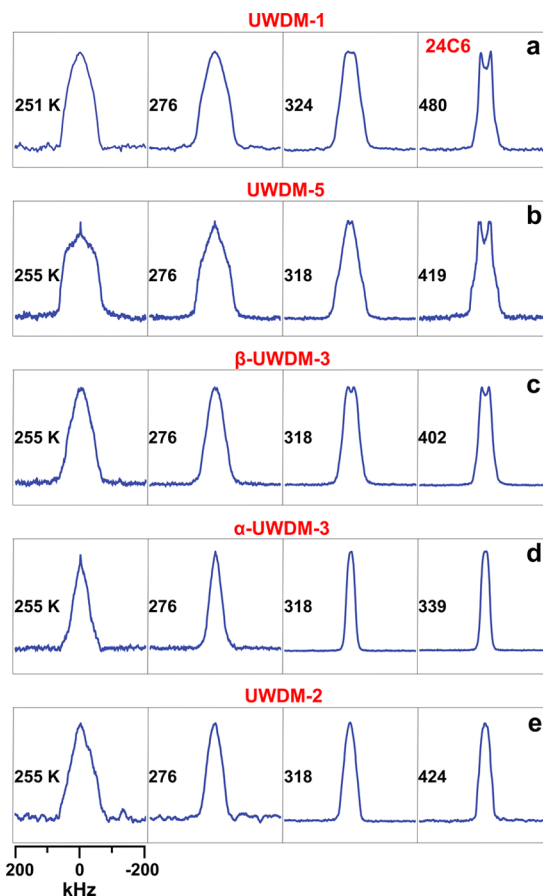


Figure 7. Experimental ^2H NMR spectra from the crown ether 24C6 interlocked in UWDM-1 (row a), UWDM-5 (row b), β -UWDM-3 (row c), α -UWDM-3 (row d), and UWDM-2 (row e), at the temperatures depicted in the figure. Reproduced with permission from refs 14 and 16. Copyrights 2014 and 2016 American Chemical Society.

acquired at the particular temperature where it actually appears. It may be concluded that the character of the lineshape evolution with temperature is similar in rows a–c, with the activation energies for R_\perp and R_\parallel being characteristic for each system.

Figures 7d,e shows selected ^2H NMR spectra from the group B systems α -UWDM-3/24C6 and UWDM-2/24C6. Up to 318 K, rows d and e exhibit pairs of spectra obtained at the same temperature. The constituents of each pair are nearly the same, and the pairs differ from one another (see also Figure S2 of the Supporting Information, parts c and d). It may be concluded that in the 255–318 K temperature range, the activation energies for R_\perp and R_\parallel are nearly the same for α -UWDM-3/24C6 and UWDM-2/24C. Above 318 K, the ^2H spectra were obtained at different temperatures for these two systems. The 339 K spectrum in row d and the 424 K spectrum in row e are visually very close to the preceding 318 K spectra. The straightforward interpretation is that the high-temperature spectra belong to the extreme motional narrowing limit. As such, they do not provide new information and may be disregarded in the context of the present discussion.

Below 276 K (second column from the left in Figure 7), the group B spectra are generally similar in appearance to the group A spectra (the shoulder issue is discussed above), except for being considerably narrower, most likely due to fast local fluctuations in the group B systems. That such motions are experienced by 24C6 residing in the tight spaces of α -UWDM-3

and UWDM-2 is not surprising. Above 276 K, the group A spectra (rows a–c) evolve into a “horn”-featuring lineshape. On the other hand, the group B spectra (rows d and e) do not evolve into such a shape.

Figure 8 shows UWDM-1 with 24C6 (row a), 22C6 (row b), and B24C6 (row c). The ^2H NMR spectra in rows a and b may

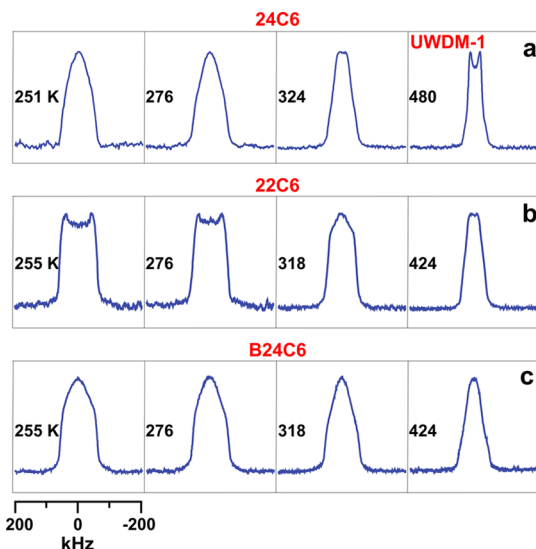


Figure 8. Experimental ^2H NMR spectra from UWDM-1 with 24C6 (part a), 22C6 (part b), and B24C6 (part c), at the temperatures depicted in the figure. Reproduced with permission from ref 15. Copyright 2015 American Chemical Society.

be included in group A; the ^2H NMR spectra in row c may be included in group B, without line-narrowing. It is interesting that unlike 24C6 in the tight spaces of α -UWDM-3 (Figure 7d) and UWDM-2 (Figure 7e), bulky B24C in UWDM-1 (Figure 8c) does not experience fast local fluctuations. Further studies are required to clarify this matter. The conclusions drawn on the basis of the selected lineshapes shown in Figures 7 and 8 are reinforced by the full lineshape evolutions shown in Figures S2, S3, S5, and S7 of the Supporting Information.

3.4.2. Quantitative Analysis. **3.4.2.1. MSM Analysis.** Typical experimental ^2H spectra of the macrocycle 24C6 and the temperatures at which they appear in the different systems are shown in Figure S4 of the Supporting Information. The annotations below each spectrum specify the best-fit parameters of the simple motional modes (separated by semicolons), which together constitute the overall model used to reproduce that spectrum. Clearly, model diversity (i.e., extensive variation in the identity of the simple motional modes and the values of the pertinent parameters) among systems is substantial. Figure S5 of the Supporting Information shows the evolution of the ^2H spectra of 24C6, 22C6, and B24C6 in UWDM-1 as a function of temperature, with the MSM models specified for each system at every temperature. Model diversity is considerable in extent, both as a function of system type and as a function of temperature. Finally, Figure S6 of the Supporting Information shows the full evolution with temperature of the ^2H spectra of 24C6 in UWDM-1, the best-fit MSM spectra, and the molecular schematics of the simple motional modes considered in obtaining the latter. For selected temperatures (160, 180, 203, and 225 K), Figure S5, column on the left, shows the models used to obtain the corresponding spectra and the pertinent best-

fit parameters. Each temperature is associated with a different model, hence a different set of parameters.

3.4.2.2. MOMD Analysis. The upper part of Figure 9 shows experimental ^2H NMR spectra of UWDM-1 with 24C6,¹⁵ which

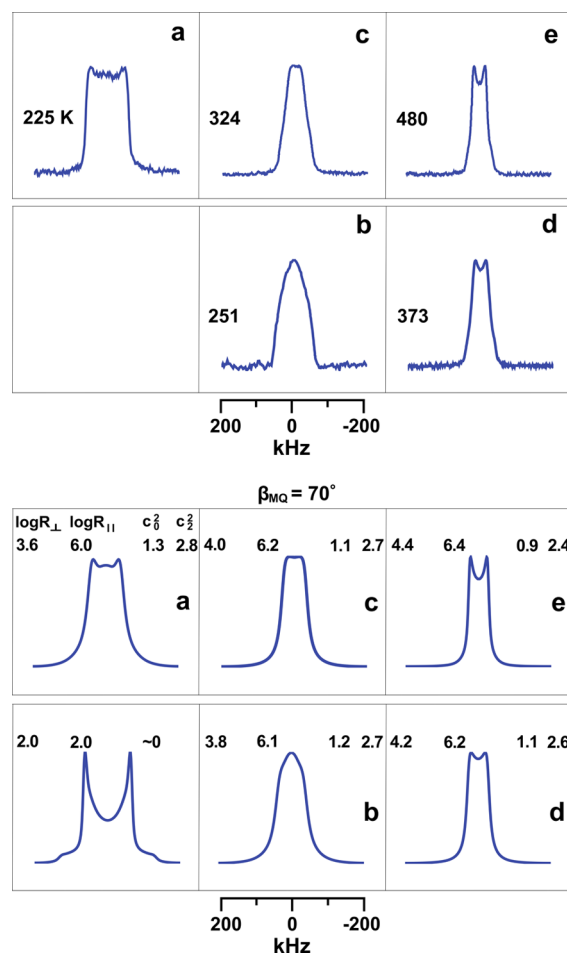


Figure 9. Upper part: experimental ^2H NMR spectra from UWDM-1 with 24C6 at 225 (a), 251 (b), 324 (c), 373 (d), and 480 K (e). Reproduced with permission from ref 15. Copyright 2015 American Chemical Society. Lower part: MOMD spectra that fit best the experimental spectra of the upper part. $\log R_{\perp}$, $\log R_{\parallel}$, c_0^2 , c_2^2 , and β_{MQ} as depicted in the figure and given in Table 2. The definition of the various parameters and additional information used in these calculations are the same as in the caption of Figure 4.

are representative of group A. The lower part shows the corresponding best-fit MOMD spectra, obtained following extensive simulations. The agreement between calculated and experimental spectra is good. The goodness-of-fit is estimated visually taking into account the independently determined sensitivity of the MOMD analysis to the various MOMD parameters and the errors in these parameters (depicted below). Currently, we do not have an automated data-fitting scheme that would provide statistical measures. The authors of refs 13–16 did not report such a scheme either. Consequently, MOMD versus MSM comparison is also conducted on the basis of visual assessment. The agreement of the MOMD spectra with the corresponding experimental spectra is comparable to the agreement of the MSM spectra with the corresponding experimental spectra – see Figure 9 for MOMD and Figures S6 and S7 for MSM.

The angle $\beta_{\text{MQ}} = 70^\circ$ gave the best overall result in the temperature range of 225–480 K; the estimated error is $\pm 2.5^\circ$. $\beta_{\text{MQ}} = 70^\circ$ is consistent with deuterium bonded to tetrahedral carbon, with the local diffusion axis pointing along the symmetry axis of the tetrahedron. This carbon atom belongs to the crown-ether ring (Figure 10a); in view of strain associated with ring

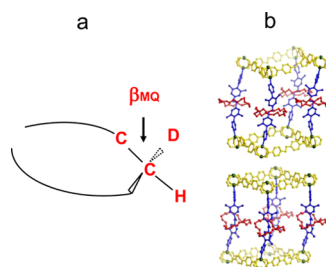


Figure 10. (a) Schematic illustration of a crown ether macrocycle with the ^2H -labeled site expanded. For illustration, the hydrogenated (using deuterium gas) carbon–carbon bond is depicted as a single bond of tetrahedral character. (b) Ball-and-stick representations of the single-crystal X-ray structures of UWDM-2 containing ADC linkers (top) and UWDM-3 containing BPDC linkers (bottom), showing portions of the corresponding interpenetrated lattice frameworks. Color key: blue – aniline axle, red – 24C6 wheel, yellow – carboxylate linkers, and green – zinc atoms. Reproduced with permission from ref 14. Copyright 2014 American Chemical Society.

closure, perfect tetrahedral symmetry is not expected. Our results should be viewed as a preference for this stereochemically relevant geometric arrangement rather than proof of tetrahedral symmetry.

The potential coefficient c_0^2 decreases from 1.3 to 0.9 and the potential coefficient c_2^2 decreases from 2.8 to 2.4 in the 225–480 K temperature range. The estimated error in c_0^2 and c_2^2 is 5%. As indicated in the Theoretical Background section, from the coefficients c_0^2 and c_2^2 one may calculate the second-rank local ordering tensor, S (eqs 4 and 5). Table 2 shows the order parameter in irreducible-tensor notation (S_0^2 and S_2^2) and in Saupe tensor notation (S_{xx} , S_{yy} , and S_{zz}), calculated from the best-fit c_0^2 and c_2^2 values of Figure 9. The estimated error in the order parameters is 7%. All of these parameters are depicted in Table 2 in the 225–480 K temperature range. The best-fit values of the diffusion rate constants, R_{\parallel} and R_{\perp} , with estimated errors of 10%, are also shown.

At 225 K, the component S_{xx} is the largest Saupe order parameter, the component S_{yy} is somewhat smaller with opposite sign, and S_{zz} is very small. This indicates x ordering with “nearly planar xy ordering”.

It is of interest to pictorially illustrate the MOMD model as applied in this study. Figure 10 does this by associating the parameters R_{\parallel} , R_{\perp} , c_0^2 , and c_2^2 with molecular features. The ^2H -labeled macrocycle is shown in Figure 10a. The bond depicted as

“C–C” was a double bond prior to hydrogenation using deuterium gas; after hydrogenation, its coordination character is in-between a single (tetrahedral) bond and a double bond (Section 3.2. (c)); within the scope of this representative display, we show it as a single bond. According to the definition of the angle β_{MQ} , the PAS of the R tensor has its z axis parallel to C–C. Usually, the faster rate constant is associated with the z axis and the slower rate constant with the x and y axes; in some cases, the reverse relationship was found to be valid.³⁸ The latter case suits the present situation as the motion of the macrocycle is most likely slower than the motion of the C–D bond. All things considered, including the effective/collective character of the MOMD mode, we associate R_{\perp} with the macrocycle and R_{\parallel} with the C–D bond.

Figure 10b shows ball-and-stick representations of the single-crystal X-ray structures of UWDM-2 containing ADC linkers (top) and UWDM-3 containing BPDC linkers (bottom), as portions of the corresponding interpenetrated lattice frameworks.¹⁴ The macrocycle 24C6 is colored in red. That the different surroundings exert different restrictions at the site of the motion of the macrocycle in the UWDM-2 lattice as compared to the UWDM-3 lattice can be assessed qualitatively by visual examination. The coefficients c_0^2 and c_2^2 provide a quantitative estimate of the strength and rhombicity of these restrictions, within the scope of the potential given by eq 4.

Both R_{\parallel} and R_{\perp} increase with increasing temperature. Based on the data shown in Figure 9 and Table 2, we calculated activation energies of 7.5 ± 0.8 kJ/mol for R_{\parallel} and 3.4 ± 0.35 kJ/mol for R_{\perp} . Both values are substantially smaller than the MSM estimates for specific simple dynamic modes.^{13–16} The MOMD results are consistent with large changes in temperature causing relatively small changes in the experimental ^2H spectra (Figures S2, S3, and S5–S7 of the Supporting Information).

Except for the activation energies for local motion, the results obtained for UWDM-1/24C6 (lower part of Figure 9 and Table 2) also refer to the other members of group A. Obtaining accurate energies for local motion for the various systems requires further investigation.

We turn now to group B, with constituents UWDM-2/24C6 and α -UWDM-3/24C6. Below 276 K, the results obtained for group A apply; above 276 K, the lineshapes change very little with a further increase in temperature. One might maintain that the extreme motional narrowing limit has been attained already at 276 K – see qualitative analysis delineated in Section 3.4.1. On the basis of quantitative analysis, this is, however, unlikely (a) in view of the group B values of R_{\parallel} and R_{\perp} at 276 K (see below) and (b) in light of previous quantitative studies of similar systems.^{36,37,39,40}

Thus, the challenge is to reproduce the ^2H lineshapes for 318 and 339 K in Figure 7d and for 318 and 424 K in Figure 7e. One can do so quite easily using axial u and spherical R . However, it is not reasonable for the local potential and the local diffusion

Table 2. Potential Coefficients, c_0^2 and c_2^2 , from Figure 9; Corresponding Order Parameters S_0^2 and S_2^2 (in Irreducible-Tensor Notation) and S_{xx} , S_{yy} , and S_{zz} (in Saupe Tensor Notation); Diffusion Rate Constants, $\log R_{\perp}$, and $\log R_{\parallel}$ from Figure 9

exp'l temp. (K)	c_0^2	c_2^2	S_0^2	S_2^2	S_{xx}	S_{yy}	S_{zz}	order type	$\log R_{\perp}$	$\log R_{\parallel}$
225	1.3	2.8	−0.034	0.652	0.416	−0.382	−0.034	x	3.6	6.0
251	1.2	2.7	−0.039	0.648	0.416	−0.377	−0.039	x	3.8	6.1
324	1.1	2.7	−0.059	0.663	0.436	−0.377	−0.059	x	4.0	6.2
373	1.1	2.6	−0.044	0.644	0.416	−0.372	−0.044	x	4.2	6.2
480	0.9	2.4	−0.054	0.633	0.414	−0.361	−0.054	x	4.4	6.4

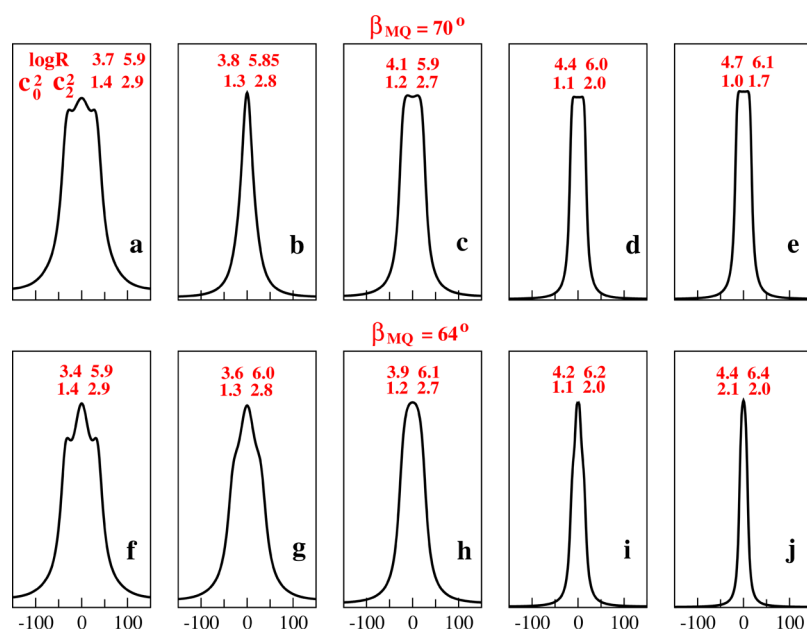


Figure 11. Simulated MOMD spectra for $\log R_\perp$, $\log R_\parallel$, c_0^2 , and c_2^2 as depicted in the figure and given in Table 3, with $\beta_{MQ} = 70^\circ$ (a–e) and $\beta_{MQ} = 64^\circ$ (f–j). The definition of the various parameters and additional information used in these calculations are the same as in the caption of Figure 4.

Table 3. Potential Coefficients, c_0^2 and c_2^2 , and Diffusion Rate Constants, $\log R_\perp$ and $\log R_\parallel$, from Figure 11f–j; Order Parameters (See Title of Table 2 for Details) Calculated from c_0^2 and c_2^2

figure	c_0^2	c_2^2	S_0^2	S_2^2	S_{xx}	S_{yy}	S_{zz}	order type	$\log R_\perp$	$\log R_\parallel$
f	1.4	2.9	−0.030	0.655	0.416	−0.386	−0.030	x	3.4	5.9
g	1.3	2.8	−0.034	0.652	0.416	−0.382	−0.034	x	3.6	6.0
h	1.2	2.7	−0.039	0.648	0.416	−0.377	−0.059	x	3.9	6.1
i	1.1	2.0	0.050	0.514	0.290	−0.340	0.049	y	4.2	6.2
j	2.1	2.0	0.289	0.352	0.071	−0.360	0.072	axial y	4.4	6.4

tensor to be more symmetrical in the highly restrictive spaces of the group B systems than in the much less restrictive spaces of the group A systems; the opposite trend is expected. Also, a spherical R tensor implies identical rates for C–D motion and macrocycle motion, which is unlikely.

Below 276 K, the best agreement between experiment and calculation is obtained for rhombic u , axial R , and $\beta_{MQ} = 70^\circ$. c_0^2 and c_2^2 decrease, whereas R_\parallel and R_\perp increase, with increasing temperature. In general agreement with these characteristics, the best results obtained for group B above 276 K are shown in Figure 11a–e. We carried out extensive simulations varying all of the parameters in small steps. The spectra of Figure 11d,e is the closest we could get to the high-temperature ^2H spectra of Figure 7d,e using $\beta_{MQ} = 70^\circ$. The agreement between calculated and experimental lineshapes is not satisfactory primarily because spectra 11d and 11e show horns, while the high-temperature spectra in Figure 7d,e do not. The horn pattern is eliminated by using the stereochemically viable alternative of $\beta_{MQ} = 64^\circ$ (cf. Section 3.2. (c)) and allowing c_0^2 to increase with increasing temperature at the high-temperature end. This is shown in Figure 11f–j, which represents a typical spectrum evolution suitable to group B.

Table 3 shows the order parameters calculated from the c_0^2 and c_2^2 values of Figure 11f–j, the c_0^2 and c_2^2 values themselves, and R_\parallel and R_\perp . Similar to the group A spectra preferential x ordering with nearly planar xy ordering prevails for the lineshapes 11f–h. On the other hand, preferential y ordering with “closely planar xy ordering” prevails for the lineshape 11i. In going from spectrum

11i to spectrum 11j, the y ordering is preserved, but it becomes axial. Thus, beyond spectrum 11h, which represents the situation at 276 K, the symmetry of the local ordering changes significantly.

The fact that the narrow feature-less spectrum in Figure 11i appears at substantially higher (simulated) temperature than the similarly looking spectrum in Figure 11b is indicative of substantially higher activation barrier for $\beta_{MQ} = 64^\circ$ (deuterium-bonded carbon atom with double-bond character) as compared to $\beta_{MQ} = 70^\circ$ (deuterium-bonded carbon atom with single-bond character).

As expected, the local diffusion rate constants, reported as $\log R_\perp$ and $\log R_\parallel$, increase with increasing temperature. Note that $\log R_\perp$ of 4.2 and 4.4 and $\log R_\parallel$ of 6.1 are smaller than their extreme motional narrowing values. The axial potential coefficient, c_0^2 , increases in going from spectrum 11i to spectrum 11j; this might appear counterintuitive. However, one has to consider the coefficients c_0^2 and c_2^2 jointly in evaluating the form/symmetry of the local potential. This can be done by considering order parameters that are defined in terms of both c_0^2 and c_2^2 , which we indeed did in discussing the data of Tables 2 and 3.

The following comment is important. As pointed out above, there exist in the field of protein dynamics by NMR methods other than MOMD for treating internal molecular mobility in the solid state; some have been developed recently.^{10–12} Many methods only treat the relaxation limit;^{11,12} in some formalisms, the spatial restraints are implicit in the geometric features;¹⁰ and SLE-based approaches represent both the motion itself and the

spatial restrictions operating on it in simple encoded forms.^{4,5} These methods cannot provide information with regard to the form of the local ordering potentials and the coordination character of the atoms that constitute the NMR probe.

4. CONCLUSIONS

The microscopic-order-macroscopic-disorder (MOMD) approach for elucidating structural dynamics by NMR lineshape analysis was applied to the case of University of Windsor Dynamic Materials of types 1, 2, α -3, β -3, and 5. The “dynamic” component is a crown ether – 24C6, 22C6, or B24C6 – labeled selectively with deuterium. ²H lineshapes have been analyzed with MOMD over temperature ranges of 220 K (on average). Two UWDM groups were identified. Group A comprises UWDM of types 1, β -3, and 5, and group B comprises UWDM-2 and α -UWDM-3. In group A, where the crown ether is less constrained spatially, C–D motion is relatively fast (R_{\parallel} in the $(1.0\text{--}2.5) \times 10^6 \text{ s}^{-1}$ range), macrocycle motion is relatively slow (R_{\perp} in the $(0.4\text{--}2.5) \times 10^4 \text{ s}^{-1}$ range), and the local potential is relatively weak and highly rhombic (c_0^2 and c_2^2 are in the 1–3 range). Within a good approximation, the deuterium-bonded C-atom has tetrahedral-carbon character. The group members differ in the activation energies for R_{\parallel} and R_{\perp} ; quantitative determination of these differences is postponed to future work.

In group B, the crown ether is considerably more constrained spatially. Below 276 K, the temperature-induced evolution is similar to that of group A. Above 276 K, the form/symmetry of the local potential differs from the form/symmetry of the group A local potential. In addition, the deuterium-bonded C-atom assumes double-bond character.

The MOMD picture of structural dynamics is general, consistent, and physically relevant; these attributes lead to new insights and new applications (e.g., see below). The MSM picture is limited in scope with regard to these characteristics.

The well-defined MOMD parameters associated consistently with a single effective/collective local motional mode can help in the design of MOF/MIM-type molecular machines. Within the scope of clean environment promotion, they could be useful for the development of MOFs for capturing carbon dioxide²⁰ and nitrogen dioxide.¹⁹

■ ASSOCIATED CONTENT

SI Supporting Information

The Supporting Information is available free of charge at <https://pubs.acs.org/doi/10.1021/acs.jpcc.0c03687>.

Illustrations of selected MOF and MIM structures (Figure S1); experimental ²H spectra from selected UWDM systems (Figures S2–S4): experimental ²H spectra and textual description of the models used to reproduce them with MSM (Figure S5); experimental ²H spectra, best-fit MSM spectra, and illustration of the various simple modes used (Figure S6); and experimental ²H spectra and corresponding best-fit MSM spectra (Figure S7) (PDF)

■ AUTHOR INFORMATION

Corresponding Authors

Eva Meirovitch – *The Mina and Everard Goodman Faculty of Life Sciences, Bar-Ilan University, Ramat-Gan 52900, Israel;*
ORCID.org/0000-0001-5117-5079; Phone: 972-3-531-8049;
Email: eva.meirovitch@biu.ac.il

Jack H. Freed – *Baker Laboratory of Chemistry and Chemical Biology, Cornell University, Ithaca, New York 14853-1301,*

United States; ORCID.org/0000-0003-4288-2585;
Phone: 607-255-3647; Email: jhf3@cornell.edu

Author

Zhichun Liang – *Baker Laboratory of Chemistry and Chemical Biology, Cornell University, Ithaca, New York 14853-1301, United States*

Complete contact information is available at:
<https://pubs.acs.org/10.1021/acs.jpcc.0c03687>

Notes

The authors declare no competing financial interest.

■ ACKNOWLEDGMENTS

This work was supported by the Israel - USA Binational Science Foundation (Grant No. 2016097 to E.M. and J.H.F.) and the Israel Science Foundation (Grant No. 469/15 to E.M.). This work was also supported by NIH/NIGMS grant P41GM103521 to J.H.F.

■ REFERENCES

- (1) Spiess, H. W. *Dynamic NMR spectroscopy*; Diehl, P.; Fluck, E.; Kosfeld, R., Eds., 1978, Vol. 15, pp 55–241.
- (2) Huang, T. H.; Skarjune, R. P.; Wittebort, R. J.; Griffin, R. G.; Oldfield, E. Restricted Rotational Isomerization in Polymethylene Chains. *J. Am. Chem. Soc.* **1980**, *102*, 7377–7379.
- (3) Batchelder, L. S.; Sullivan, C. E.; Jelinski, L. W.; Torchia, D. A. Characterization of Leucine Side-Chain Reorientation in Collagen Fibrils by Solid-State ²H NMR. *Proc. Natl. Acad. Sci. U. S. A.* **1982**, *79*, 386–389.
- (4) Vold, R. L.; Hoatson, G. L. Effects of Jump Dynamics on Solid State Nuclear Magnetic Resonance Line Shapes and Spin Relaxation Times. *J. Magn. Res.* **2009**, *198*, 57–72.
- (5) Echodu, D.; Goobes, G.; Shajani, Z.; Pederson, K.; Meints, G.; Varani, G.; Drobny, G. Furanose Dynamics in the *HhaI* Methyltransferase Target DNA Studied by Solution and Solid-State NMR Relaxation. *J. Phys. Chem. B* **2008**, *112*, 13934–13944.
- (6) *Solid-State NMR Studies of Biopolymers*; McDermott, A. E.; Polenova, T., Eds.; John Wiley and Sons: U.K., 2010.
- (7) Krushelnitsky, A.; Reichert, D.; Saalwächter, K. Solid-State NMR Approaches to Internal Dynamics of Proteins: from Picoseconds to Microseconds and Seconds. *Acc. Chem. Res.* **2013**, *46*, 2028–2036.
- (8) Meirovitch, E.; Liang, Z.; Freed, J. H. Protein Dynamics in the Solid State from ²H NMR Line Shape Analysis: A Consistent Perspective. *J. Phys. Chem. B* **2015**, *119*, 2857–2868.
- (9) Schanda, P.; Ernst, M. Studying Dynamics by Magic-Angle-Spinning Solid-State NMR Spectroscopy: Principles and Applications to Biomolecules. *Prog. Nucl. Magn. Reson. Spectrosc.* **2016**, *96*, 1–46.
- (10) Au, D. F.; Ostrovski, D.; Fu, R.; Vugmeyster, L. Solid-State NMR Reveals a Comprehensive View of the Dynamics of the Flexible Disordered N-Terminal Domain of Amyloid- β Fibrils. *J. Biol. Chem.* **2019**, *294*, 5840–5853.
- (11) Busi, B.; Yarava, J. R.; Hofstetter, A.; Salvi, N.; Cala-De Paepe, D.; Lewandowski, J. R.; Blackledge, M.; Emsley, L. Probing Protein Dynamics Using Multifield Variable Temperature NMR Relaxation and Molecular Dynamics Simulation. *J. Phys. Chem. B* **2018**, *122*, 9697–9702.
- (12) Smith, A. A.; Ernst, M.; Meier, B. H.; Ferrage, F. Reducing Bias in the Analysis of Solution-State NMR Data with Dynamics Detectors. *J. Chem. Phys.* **2019**, *151*, 034102–034115.
- (13) Vukotic, V. N.; Harris, K. J.; Zhu, K.; Schurko, R. W.; Loeb, S. J. Metal-Organic Frameworks with Dynamic Interlocked Components. *Nat. Chem.* **2012**, *4*, 456–460.
- (14) Zhu, K.; Vukotic, V. N.; O’Keefe, C. A.; Schurko, R. W.; Loeb, S. J. Metal-Organic Frameworks with Mechanically Interlocked Pillars: Controlling Ring Dynamics in the Solid-State via a Reversible Phase Transition. *J. Am. Chem. Soc.* **2014**, *136*, 7403–7409.

- (15) Vukotic, V. N.; O'Keefe, C. A.; Zhu, K.; Harris, K. J.; To, C.; Schurko, R. W.; Leob, S. J. Mechanically Interlocked Linkers inside Metal-Organic Frameworks: Effect of Ring Size on Rotational Dynamics. *J. Am. Chem. Soc.* **2015**, *137*, 9643–9651.
- (16) Farahani, N.; Zhu, K.; O'Keefe, C. A.; Schurko, R. W.; Leob, S. J. Thermally Driven Dynamics of a Rotaxane Wheel about an Imidazolium Axle inside a Metal-Organic Framework. *ChemPlusChem* **2016**, *81*, 836–841.
- (17) Li, J.; Han, X.; Zhang, X.; Sheveleva, A. M.; Cheng, Y.; Tuna, F.; McInnes, E. J.; McPherson, L. J. M.; Teat, S. J.; Daemen, L. L.; Ramirez-Cuesta, A. J.; Schröder, M.; Yang, S. Capture of Nitrogen Dioxide and Conversion to Nitric Acid in a Porous Metal-Organic Framework. *Nat. Chem.* **2019**, *11*, 1085–1090.
- (18) Liu, J.; Wei, Y.; Zhao, Y. Trace Carbon-Dioxide Capture by Metal-Organic Frameworks. *Sustain. Chem. Eng.* **2019**, *7*, 82–93.
- (19) Vornholt, S. M.; Morris, R. E. Separating out the Middle. *Nat. Mater.* **2019**, *18*, 910–911.
- (20) Ashworth, C. Nanocavities Cause a Stir. *Nat. Rev. Mater.* **2018**, *3*, 458.
- (21) Ferrarini, A.; Nordio, P.-L.; Moro, G. J.; Crepeau, R. H.; Freed, J. H. A Theoretical Model of Phospholipid Dynamics in Membranes. *J. Chem. Phys.* **1989**, *91*, 5707–5721.
- (22) Cassol, R.; Ge, M.-T.; Ferrarini, A.; Freed, J. H. Chain Dynamics and the Simulation of Electron Spin Resonance Spectra from Oriented Phospholipid Membranes. *J. Phys. Chem. B* **1997**, *101*, 8782–8789.
- (23) Meirovitch, E.; Nayeem, A.; Freed, J. H. Analysis of protein-lipid interactions based on model simulations of electron spin resonance spectra. *J. Phys. Chem.* **1984**, *88*, 3454–3465.
- (24) Meirovitch, E.; Liang, Z.; Freed, J. H. Protein Dynamics in the Solid State from ^2H NMR Lineshape Analysis. II MOMD Applied to C-D and C- CD_3 Probes. *J. Phys. Chem. B* **2015**, *119*, 14022–14032.
- (25) Meirovitch, E.; Liang, Z.; Freed, J. H. MOMD Analysis of NMR Lineshapes from A β -Amyloid Fibrils: A New Tool for Characterizing Molecular Environments in Protein Aggregates. *J. Phys. Chem. B* **2018**, *122*, 4793–4801.
- (26) Meirovitch, E.; Liang, Z.; Freed, J. H. Phenyl-Ring Dynamics in Amyloid Fibrils and Proteins: The Microscopic-Order-Macroscopic-Disorder Perspective. *J. Phys. Chem. B* **2018**, *122*, 8675–8684.
- (27) Meirovitch, E.; Liang, Z.; Freed, J. H. Protein Dynamics in the Solid State from ^2H NMR Line Shape Analysis. III. MOMD in the Presence of Magic Angle Spinning. *Solid State Nucl. Magn. Reson.* **2018**, *89*, 35–44.
- (28) Polnaszek, C. F.; Bruno, G. V.; Freed, J. H. ESR Line shapes in the Slow-Motional Region: Anisotropic Liquids. *J. Chem. Phys.* **1973**, *58*, 3185–3199.
- (29) Polnaszek, C. F.; Freed, J. H. Electron Spin Resonance Studies of Anisotropic Ordering, Spin Relaxation, and Slow Tumbling in Liquid Crystalline Solvents. *J. Phys. Chem.* **1975**, *79*, 2283–2306.
- (30) Lin, W. J.; Freed, J. H. Electron Spin Resonance Studies of Anisotropic Ordering, Spin Relaxation, and Slow Tumbling in Liquid Crystalline Solvents: 3. Smectics. *J. Phys. Chem.* **1979**, *83*, 379–401.
- (31) Polimeno, A.; Zerbetto, M.; Abergel, D. Stochastic Modeling of Macromolecules in Solution I. Relaxation Processes Time-Scales. *J. Chem. Phys.* **2019**, *150*, 184107.
- (32) Polimeno, A.; Zerbetto, M.; Abergel, D. Stochastic Modeling of Macromolecules in Solution II. Spectral Densities. *J. Chem. Phys.* **2019**, *150*, 184108.
- (33) Tchaicheeyan, O.; Freed, J. H.; Meirovitch, E. Local Ordering at Mobile Sites in Proteins from Nuclear Magnetic Resonance Relaxation: The Role of Site Symmetry. *J. Phys. Chem. B* **2016**, *120*, 2886–2898.
- (34) Polimeno, A.; Freed, J. H. *A Many-Body Stochastic Approach to Rotational Motions in Liquids*. In *Advances in Chemical Physics LXXXIII*; Prigogine, I.; Rice, S. A., Eds.; Wiley: NY, 1993, 89–204.
- (35) Schneider, D. J.; Freed, J. H. Calculating Slow Motional Magnetic Resonance Spectra: A User's Guide. In *Biological Magnetic Resonance*; Plenum: New York, 1989, Vol. 8, pp 1–76.
- (36) Schadt, R. J.; Cain, E. J.; English, A. D. Simulation of one-dimensional deuteron NMR line shapes. *J. Phys. Chem.* **1993**, *97*, 8387–8392.
- (37) Ratcliffe, C. I.; Buchanan, G. W.; Denike, J. K. Dynamics of 12-Crown-4 Ether in Its LiNCS Complex as Studied by Solid-State ^2H NMR. *J. Am. Chem. Soc.* **1995**, *117*, 2900–2906.
- (38) Liang, Z.; Lou, Y.; Freed, J. H.; Columbus, L.; Hubbell, W. L. A Multifrequency Electron Resonance Study of T4 Lysozyme Dynamics Using the Slowly Relaxing Local Structure Model. *J. Phys. Chem. B* **2004**, *108*, 17649–17659.
- (39) Ratcliffe, C. I.; Ripmeester, J. A.; Buchanan, G. W.; Denike, J. K. A Molecular Merry-Go-Around: Motion of the Large Macrocyclic Molecule 18-Crown-6 in its Solid Complexes Studied by H NMR. *J. Am. Chem. Soc.* **1992**, *114*, 3294–3299.
- (40) Nishikiori, S.; Ratcliffe, C. I.; Ripmeester, J. A. Solid-State NMR Study of Cyclohexane Reorientation and Inversion in N-Methyl-1,3-Diaminopropane(cadmium(II) Tetracyanonickelate(II)-Cyclohexane (2/1) Clathrate. *J. Phys. Chem.* **1990**, *94*, 8098–8102.